Nanophotonic projection system

Firooz Aflatouni,[1,2,*] **Behrooz Abiri,**[1] **Angad Rekhi,**[1] **and Ali Hajimiri**[1]

[1]*Department of Electrical Engineering, California Institute of Technology, Pasadena, California 91125, USA*

[2]*Department of Electrical and Systems Engineering, University of Pennsylvania, Philadelphia, Pennsylvania 19104, USA*

[*]*firooz@seas.upenn.edu*

Abstract: Low-power integrated projection technology can play a key role in development of low-cost mobile devices with built-in high-resolution projectors. Low-cost 3D imaging and holography systems are also among applications of such a technology. In this paper, an integrated projection system based on a two-dimensional optical phased array with fast beam steering capability is reported. Forward biased p-i-n phase modulators with 200MHz bandwidth are used per each array element for rapid phase control. An optimization algorithm is implemented to compensate for the phase dependent attenuation of the p-i-n modulators. Using rapid vector scanning technique, images were formed and recorded within a single snapshot of the IR camera.

© 2015 Optical Society of America

OCIS codes: (110.5100) Phased-array imaging systems; (120.2040) Displays; (110.2990) Image formation theory; (130.6622) Subsystem integration and techniques.

References and links

1. X. Zhao, Z. L. Fang, J. C. Cui, X. Zhang, and G. G. Mu, "Illumination system using LED sources for pocket size projectors," Appl. Opt. **46**(4), 522–526 (2007).
2. Y. C. Huang and J. W. Pan, "High contrast ratio and compact-sized prism for DLP projection system," Opt. Express **22**(14), 17016–17029 (2014).
3. P. F. McManamon, T. A. Dorschner, D. L. Corkum, L. J. Friedman, D. S. Hobbs, M. Holz, S. Liberman, H. Q. Nguyen, D. P. Resler, R. C. Sharp, and E. A. Watson, "Optical phased array technology," Proc. IEEE **84**(2), 268–297 (1996).
4. B. Abiri, F. Aflatouni, A. Rekhi, and A. Hajimiri, "Electronic two-dimensional beam steering for integrated optical phased arrays," in Proceedings of the Optical Fiber Communication Conference (OFC), paper M2K.7 (2014).
5. F. Aflatouni and H. Hashemi, "An electronically controlled semiconductor laser phased array," in IEEE Microwave Symposium Digest (MTT), WEPN-6 (2012).
6. N. Satyan, W. Liang, F. Aflatouni, A. Yariv, A. Kewitsch, G. Rakuljic, and H. Hashemi, "Phase-controlled apertures using heterodyne optical phase-locked loops," IEEE Photon. Technol. Lett. **20**(11), 897–899 (2008).
7. J. K. Doylend, M. J. R. Heck, J. T. Bovington, J. D. Peters, L. A. Coldren, and J. E. Bowers, "Free-space beam steering in two dimensions using a silicon optical phased array," in Proceedings of the Optical Fiber Communication Conference (OFC), OM2J (2012).
8. K. Van Acoleyen, H. Rogier, and R. Baets, "Two-dimensional optical phased array antenna on silicon-on-insulator," Opt. Express **18**(13), 13655–13660 (2010).
9. J. Sun, E. Timurdogan, A. Yaacobi, E. Shah Hosseini, and M. R. Watts, "Large-scale nanophotonic phased array," Nature **493**(7431), 195–199 (2013).
10. B. W. Yoo, M. Megens, T. Chan, T. Sun, W. Yang, C. J. Chang-Hasnain, D. A. Horsley, and M. C. Wu, "Optical phased array using high contrast gratings for two dimensional beamforming and beamsteering," Opt. Express **21**(10), 12238–12248 (2013).
11. A. Natarajan, A. Komijani, and A. Hajimiri, "A fully integrated 24-GHz phased-array transmitter in CMOS," IEEE J. Solid-State Circ. **40**(12), 2502–2514 (2005).

#234944 Received 13 Apr 2015; revised 23 Jun 2015; accepted 10 Jul 2015; published 4 Aug 2015
© 2015 OSA

12. K. Sengupta, and A. Hajimiri, "A 0.28THz 4×4 power-generation and beam-steering array," in Proceedings of the IEEE International Solid-State Circuits Conference, 15.3, (2012), pp. 256–257.
13. W. Zhang, "LIDAR-based road and road-edge detection," in Proceedings of the IEEE Intelligent Vehicles Symposium, WeE1.12 (2010).
14. W. Liang, N. Satyan, F. Aflatouni, A. Yariv, A. Kewitsch, G. Rakuljic, and H. Hashemi, "Coherent beam combining with multi-level optical phase locked loops," J. Opt. Soc. Am. B **24**(12), 2930–2939 (2007).
15. J. Goodman, *Introduction to Fourier Optics* (McGraw-Hill, 1996).
16. A. Novack, Y. Liu, R. Ding, M. Gould, T. Baehr-Jones, Q. Li, Y. Yang, Y. Ma, Y. Zhang, K. Padmaraju, K. Bergman, A. E. J. Lim, G. Q. Lo, and M. Hochberg, "A 30 GHz silicon photonic platform," Proc. SPIE 8781, 878107 (2013).
17. L.D. Landau and E.M. Lifshitz, *Electrodynamics of Continuous Media*, 2nd ed. (Perganom Press, 1982).

1. Introduction

Small form-factor optical projectors continue to be an integral part of consumer electronics. It is not difficult to envision mobile devices equipped with low power yet high resolution microchip video projectors in near future [1]. In addition, low-cost and low power design enables wide range use of miniaturized projectors in portable low-cost 3D imaging and holography systems as well as gaming and entertainment industry. Conventionally, optical projectors are implemented using digital light processing (DLP), light emitting diode (LED) based DLP, liquid crystal display (LCD), and liquid crystal on silicon (LCOS) technologies. In a DLP projector, the projector lamp illuminates the DLP chip surface which consists of a large array of micro mirrors. Each mirror is digitally controlled and can either reflect the light into the lens (state 'on') or away from the lens (state 'off'). Since the lamp in DLP projectors is inefficient and bulky, it has been replaced with efficient LEDs in more recently manufactured DLP projectors. In LCD projectors, the pixels are set to 'on' and 'off' states using parallel LCD panels. The LCOS technology is a hybrid of LCD and DLP technologies since it uses mirrors to reflect the light and uses LCD panels to block light. Despite a few disadvantages, overall, the DLP technology has better optical efficiency and projection performance than other display systems [2]. However, even with LED based light sources, a DLP projector requires a lens, often a prism, and is inefficient due to waste of optical power by micro-mirrors in 'off' state.

Optical phased array technology can also be used to implement projection systems. Although optical phased arrays (OPA) have been studied [3–9], they have not been widely used compared to their electrical counterparts [11, 12]. However, recent advancements in integrated photonic platforms have enabled realization of reliable and compact optical phased arrays with applications in communication, LIDAR, imaging, tracking, targeting, switched fabric networks, routers, and sensing. Today, light detection and ranging (LIDAR) with beam steering capability plays a key role in autonomous vehicle technology [13].

In this paper, we report an efficient integrated projection system based on a fast steering optical phased array. The proposed architecture can project an image by vector or raster scan of the beam spot on the screen without use of a lens or any other optical components. This allows the entire projection system to be integrated on a single photonic chip with no mechanical movements at all. The phase shifters of the OPA are p-i-n phase modulators with bandwidth of 200MHz enabling ultra-fast beam steering. Using the proposed integrated 4×4 OPA, image and video projections are demonstrated. An optimization algorithm is implemented to compensate for the phase dependent attenuation of the p-i-n modulators enabling high quality yet fast beam steering. Due to low power consumption, compact size, and low cost of mass production, this integrated projection solution lends itself more towards being utilized in mobile devices.

#234944 Received 13 Apr 2015; revised 23 Jun 2015; accepted 10 Jul 2015; published 4 Aug 2015
© 2015 OSA

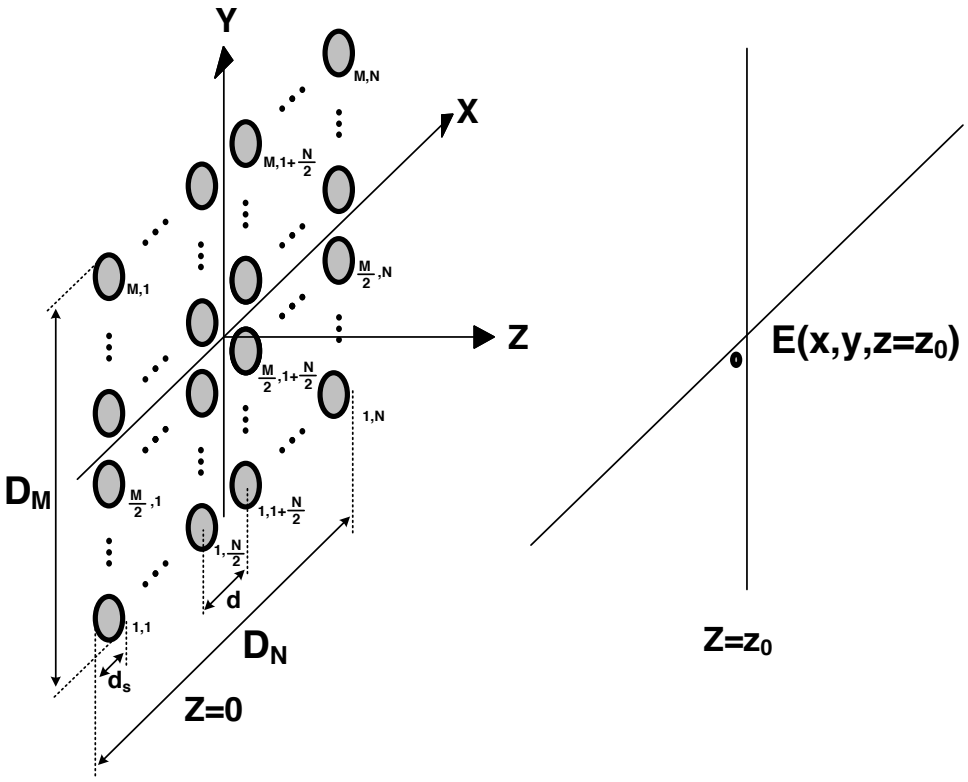

Fig. 1. The $M \times N$-element optical phased array.

2. Integrated optical phased arrays

An optical phased array consists of an array of photonic antennas that emit at the same frequency. The phase of the emitted optical wave from each antenna can be independently adjusted enabling control of the far-field wave front. Generally, there are two types of optical phased arrays. One scheme includes phase locking of an array of lasers to a stabilized reference laser using electro-optic phase locked loops (EOPLL) and offset the phase of individual array elements to perform beam forming and steering [5, 6]. In this case, a high power beam may be formed since by coherent locking of all laser elements, the total power of the output beam could be as high as the total power of all laser elements together and an intensity that increases with the square of the number of elements for a fixed space array. However, phase locking of individual lasers to a reference laser could be a challenging task. Moreover, the residual phase noise of laser elements reduces the power combining efficiency as the number of elements increases [14]. Similar to conventional electrical phased arrays, optical phased arrays can be implemented by having a single laser source and multiple phase shifters. In this case, the laser output is divided into multiple optical branches with an independently controlled optical phase shifter placed on each branch. An optical antenna (*e.g.* grating coupler or edge coupler) is placed at the end of each branch forming an array of emitters. By adjusting these phase shifters a controllable coherent optical wave front can be formed [4]. These phase shifters can be implemented as passive delay/phase elements [9], or active phase shifters [4, 7, 9]. In this scheme, no EOPLL is required. Moreover, in the absence of the residual phase noise of EOPLLs, the OPA

#234944 Received 13 Apr 2015; revised 23 Jun 2015; accepted 10 Jul 2015; published 4 Aug 2015
© 2015 OSA

can incorporate a large number of radiating elements. Therefore, this scalable OPA architecture is more suitable for implementation of a high resolution projection system.

In order to perform a rapid beam steering required for image formation using raster or vector scanning, phase shifters with fast electro-optic response are required. Although OPAs based on thermo-optic phase shifters have been demonstrated [9], the large thermal time constant associated with these phase shifters limits the maximum beam steering rate. MEMS based phase shifters enable the realization of arrays with large fill-factors [10]. However, their large mechanical time constant presents a practical challenge in utilizing them for OPA based projection systems. The p-n or p-i-n junction based phase shifters have a much faster electro-optic response compared to thermo-optic or opto-mechanical phase shifters and are better candidates for implementation of the OPA based projection systems.

Figure 1 shows a two-dimensional optical phased array where $M \times N$ radiating elements with a physical aperture which is d_s on its side are spaced apart by d along the x and y axis. Assuming Gaussian beam profile for all elements and considering radiation along the z axis at wavelength λ_0, the electric field for each element on the plane of the phased array $(z = 0)$ can be written as

$$E_{mn}(x,y,0) = E_{mn,0} e^{jm\Delta\phi_m} e^{jn\Delta\phi_n} e^{\frac{-4}{d_s^2}[(x-md)^2+(y-nd)^2]}, \tag{1}$$

where $E_{mn,0}$, m, n, $\Delta\phi_m$, and $\Delta\phi_n$ are the element field constant coefficient, element index along x axis, element index along y axis, and the constant phase difference between adjacent elements along the x and y axis, respectively. In this case, using the Fraunhofer far field approximation [15], and assuming all elements to have the same filed constant coefficient of $E_{mn,0} = E_0$, the far field intensity of the electric field at $z = z_0$ can be calculated as

$$I(x,y,z_0) = \frac{E_0^2 d_s^4 \pi^2}{16\lambda_0^2 z_0^2} e^{\frac{-\pi^2 d_s^2}{2\lambda_0^2 z_0^2}(x^2+y^2)} \times |AF_x|^2 \times |AF_y|^2. \tag{2}$$

where $AF_x = \sum_{k=1}^{M} e^{j(\frac{2\pi d}{\lambda_0 z_0}x - \Delta\phi_m)k}$ and $AF_y = \sum_{k=1}^{N} e^{j(\frac{2\pi d}{\lambda_0 z_0}y - \Delta\phi_n)k}$ are normalized array factors along x and y axis, respectively and can be calculated as

$$|AF_x| = \frac{sin[M(\frac{\pi d}{\lambda_0 z_0}x - \frac{\Delta\phi_m}{2})]}{sin[\frac{\pi d}{\lambda_0 z_0}x - \frac{\Delta\phi_m}{2}]}, \quad and \quad |AF_y| = \frac{sin[N(\frac{\pi d}{\lambda_0 z_0}y - \frac{\Delta\phi_n}{2})]}{sin[\frac{\pi d}{\lambda_0 z_0}y - \frac{\Delta\phi_n}{2}]}. \tag{3}$$

Equation (3) indicates that by adjusting $\Delta\phi_m$ and $\Delta\phi_n$, the formed beam can be steered in x and y directions, respectively. Also, the spot size formed on a screen placed at $z = z_0$ is inversely proportional to the array area, $A = MNd^2$. Moreover, the projection area inside which the beam can be steered, is proportional to $\frac{\lambda_0 z_0}{d_s}$.

3. Amplitude-phase coupling effect

Consider the case that the amplitude of phased array elements are not the same. This is for example the case where p-n or p-i-n junction based phase shifters are used in the phased array. Based on Kramers-Kronig relations [17], the insertion loss of these modulators is proportional to the amount of the generated phase shift. The normalized array factor for the 2D phased array in Fig. 1 with unequal electric field amplitudes is written as

$$AF = \frac{1}{E_0} \sum_{k=1}^{M} \sum_{k'=1}^{N} E_{mn} e^{j(\frac{2\pi d}{\lambda_0 z_0}x - \Delta\phi_m)k} e^{j(\frac{2\pi d}{\lambda_0 z_0}y - \Delta\phi_n)k'}. \tag{4}$$

#234944 Received 13 Apr 2015; revised 23 Jun 2015; accepted 10 Jul 2015; published 4 Aug 2015
© 2015 OSA

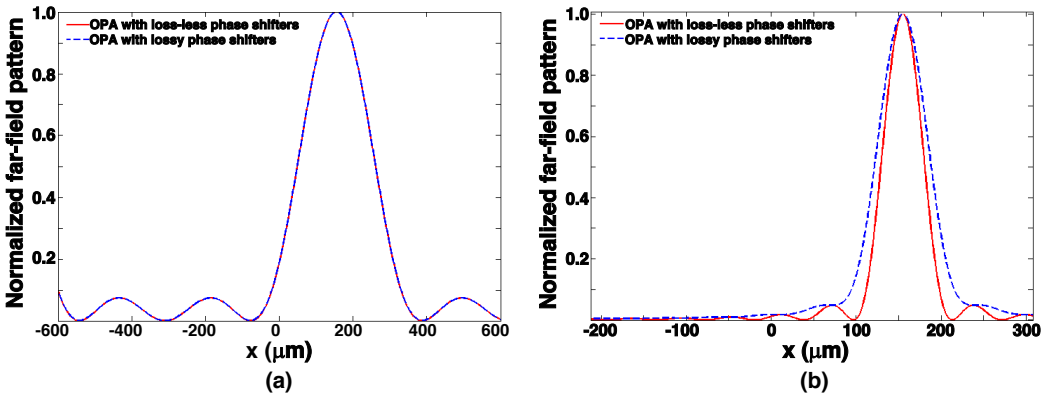

Fig. 2. The cross section of the array patterns formed at $z_0 = 3cm$ plane for an OPA with $d = 50\mu m$ and $\lambda = 1.55\mu m$ for both loss-less and lossy phase shifters. (a)$M = N = 4$, $\alpha = \frac{\pi}{8}[\frac{1}{rad}]$, $\Delta\phi_m = \Delta\phi_n = \frac{\pi}{3}[rad]$, and (b)$M = N = 16$, $\alpha = \frac{3\pi}{16}[\frac{1}{rad}]$, $\Delta\phi_m = \Delta\phi_n = \frac{\pi}{3}$ [rad].

Assuming that the electric filed amplitude loss of the phase modulator increases linearly with the amount of the phase shift, the electric filed magnitude for element kk' can be modeled as

$$E_{kk'} = E_0(1-\alpha k\phi_m)(1-\alpha k'\phi_n), \tag{5}$$

where α is the phase dependent loss coefficient in rad^{-1}. Combining Eqns. (4) and (5) results in

$$AF = \underbrace{\sum_{k=1}^{M}(1-\alpha k\phi_m)e^{j(\frac{2\pi d}{\lambda_0 z_0}x-\Delta\phi_m)k}}_{AF_{x,u}} \times \underbrace{\sum_{k'=1}^{N}(1-\alpha k'\phi_n)e^{j(\frac{2\pi d}{\lambda_0 z_0}y-\Delta\phi_n)k'}}_{AF_{y,u}}. \tag{6}$$

where $AF_{x,u}$ and $AF_{y,u}$ are the 1D array factors for the 2D phased array with unequal field amplitudes per element. Using the following identities

$$\sum_{k=1}^{M} q^k = q\frac{q^M-1}{q-1}, \quad and \quad \sum_{k=1}^{M} kq^k = q\frac{1-(M+1)q^M+Mq^{M+1}}{(1-q)^2}, \tag{7}$$

the magnitude squared of $AF_{x,u}$ and $AF_{y,u}$ can be written as

$$\begin{aligned} |AF_{x,u}|^2 &= |AF_x|^2 \times \{(1-\frac{M+1}{2}\alpha\phi_m)^2 + \frac{\alpha^2\phi_m^2}{4}[cotan(u_m) - Mcotan(Mu_m)]^2\}, \\ |AF_{y,u}|^2 &= |AF_y|^2 \times \{(1-\frac{N+1}{2}\alpha\phi_n)^2 + \frac{\alpha^2\phi_n^2}{4}[cotan(u_n) - Ncotan(Nu_n)]^2\}, \end{aligned} \tag{8}$$

where u_m and u_n are defined as $(\frac{\pi d}{\lambda_0 z_0}x - \frac{\Delta\phi_m}{2})$ and $(\frac{\pi d}{\lambda_0 z_0}y - \frac{\Delta\phi_n}{2})$, respectively. Equation (8) shows that the array factor of the array with linear phase dependent loss per element can be written as the array factor of the equivalent uniform array times a positive loss dependent factor. For this case, it can be shown that as long as $\alpha \le \frac{1}{M\phi_m}$ and $\alpha \le \frac{1}{N\phi_n}$, the main lobe of this lossy array is aligned with that of the equivalent uniform loss-less array and can be steered with exact same per-element phase settings. Figure 2 shows two examples of this case.

#234944 Received 13 Apr 2015; revised 23 Jun 2015; accepted 10 Jul 2015; published 4 Aug 2015
© 2015 OSA

4. Proposed integrated optical phased array with per-channel high speed phase control

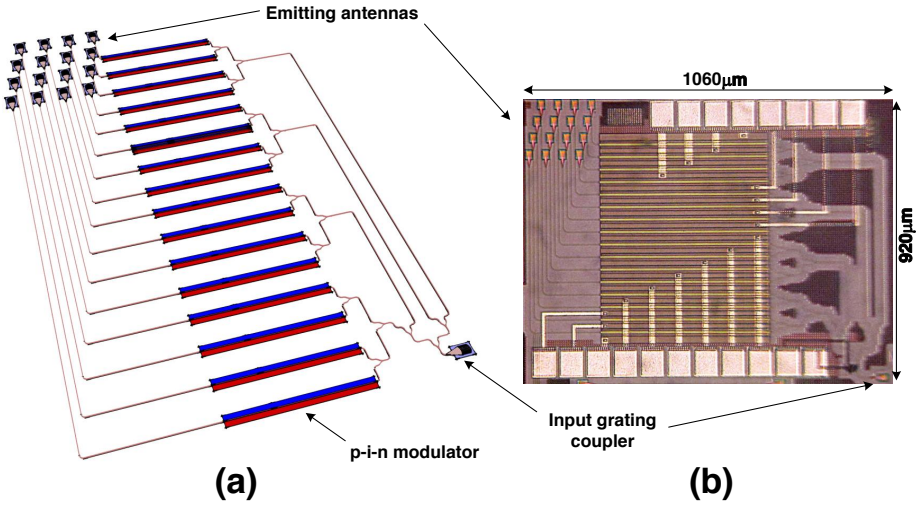

Fig. 3. (a) The structure of the reported 4×4 integrated optical phased array with per-channel high speed phase control and (b) the chip micro-photograph of the fabricated OPA.

Figure 3(a) shows the structure of the reported optical phased array. The light is coupled into the input grating coupler through a single-mode optical fiber and then is guided to a Y-junction splitter network through silicon nano-waveguides. The splitter network uniformly splits and guides the coupled light into 16 p-i-n phase modulators. The phase modulated optical waves are then guided to the radiating antenna (grating coupler) array. The radiating elements are arranged in a 4×4 parallelogram lattice in order to accommodate the optical routing. The center-to-center spacing between adjacent radiation element is $50\mu m$. The photonic micro-photograph is shown in Fig. 3(b). The total area of the fabricated micro-projector chip is less than $1mm^2$.

The cross section of the phase modulator and its propagation mode profile are depicted in Fig. 4(a) and (b), respectively. The phase modulator is a p-i-n diode formed on a strip loaded optical waveguide that operates in forward bias. As more current passes through the diode, more free carriers are injected into the waveguide. Interaction of these free carriers with the optical field changes the effective index of the waveguide altering the phase of the optical wave propagating in the modulator. The lifetime of the carriers in the modulator waveguide is about 0.7ns resulting in more than 200MHz modulation bandwidth. Therefore, the forward biased p-i-n phase modulator allows much faster phase control compared to a thermal phase shifter and hence enables fast beam steering necessary in projection. The measured I_π of the p-i-n phase modulators is about 10mA.

Based on the Kramers-Kronig relations, the optical insertion loss of carrier injection based phase modulators is directly related to the amount of optical phase shift introduced by the modulator. The measured excess attenuation of typical p-i-n modulator in our design versus modulator current is depicted in Fig. 4(c), where a linear fit to the data points results in phase-to-amplitude coupling factor (defined in Eqn. (5)) of $\alpha = \frac{1}{8\pi}\ [rad^{-1}]$. In this case, following the analysis presented in section 2 and for $N = M = 4$, it can be seen that as long as the phase increments between array elements satisfies $\Delta\phi_m, \Delta\phi_n \leq 2\pi$, the main lobe of our proposed array is aligned with the equivalent uniform loss-less array and hence, the same element phase settings may be used to steer the beam to the desired angles. However, fabrication process

#234944 Received 13 Apr 2015; revised 23 Jun 2015; accepted 10 Jul 2015; published 4 Aug 2015
© 2015 OSA

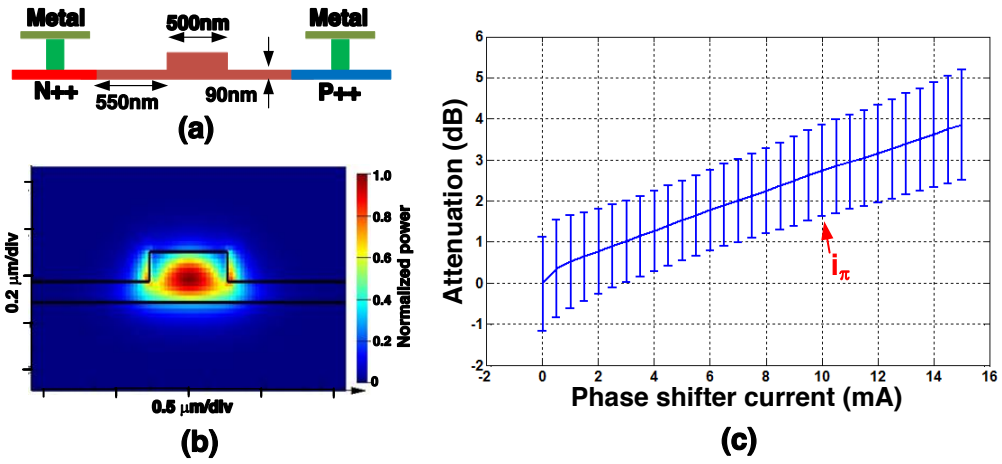

Fig. 4. (a) The cross section of the p-i-n phase modulator used in the proposed OPA, (b) the propagation mode profile of the modulator, and (c) the measured excess attenuation of the p-i-n modulators in proposed OPA.

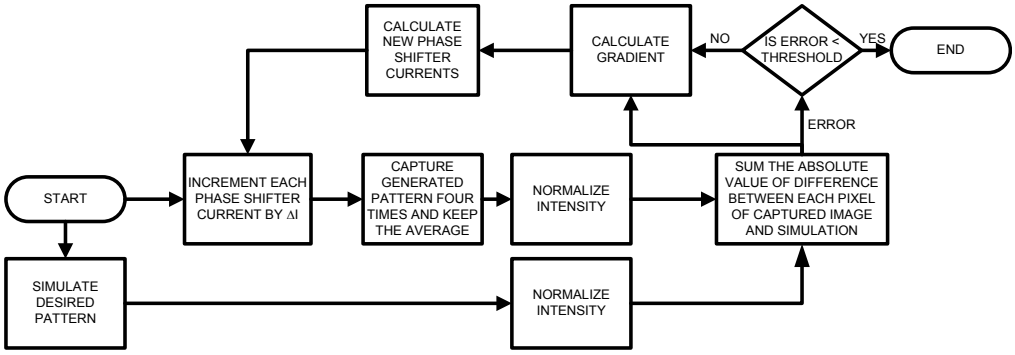

Fig. 5. The flowchart of the optimization process.

variations can result in different coupling factors for different p-i-n phase modulators. Figure 4(c) shows the variations in insertion loss of different p-i-n modulators used in the fabricated phased array. The error bars on this graph represent the range of the measured insertion loss of all 16 p-i-n modulators at each bias current. These variations result in different phase-to-amplitude coupling factors for different p-i-n modulators in the OPA. In order to compensate for these undesired variations, a calibration process is required. In the calibration phase, for each desired steering angle, the per-modulator phase setting of the equivalent uniform loss-less OPA is used as the initial point. Then an optimization algorithm is used to find a set of currents required for all phase modulators to minimize the error in the steering angle compared to the uniform loss-less OPA.

In the optimization process, first the image captured by the IR camera corresponding to the main lobe of the phased-array pattern is compared against that of a simulated uniform loss-less phased-array pattern. Since the dynamic range of the camera is limited and some saturation may occur, the simulation pattern is adjusted to account for saturation. The optimization error is defined as the pixel-wise Euclidean distance between the simulated pattern and the captured

#234944 Received 13 Apr 2015; revised 23 Jun 2015; accepted 10 Jul 2015; published 4 Aug 2015
© 2015 OSA

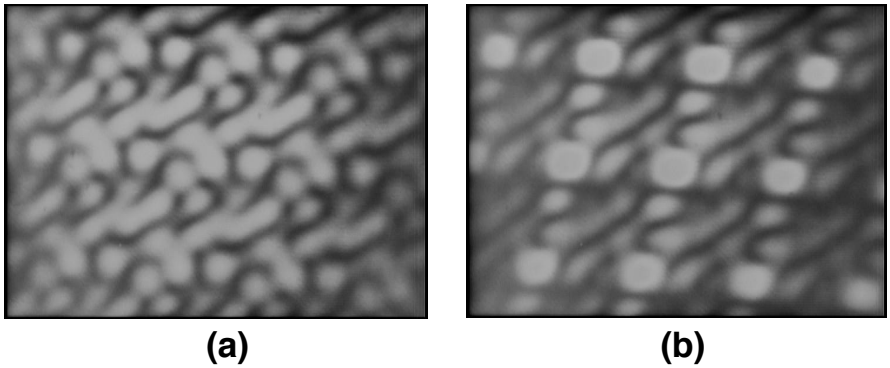

Fig. 6. The pattern of the OPA for zero relative phase setting ($\Delta\phi_m = \Delta\phi_n = 0$) captured using FJW View-R-Scope 85400A IR camera;(a) before gradient decent optimization, and (b) after gradient decent optimization.

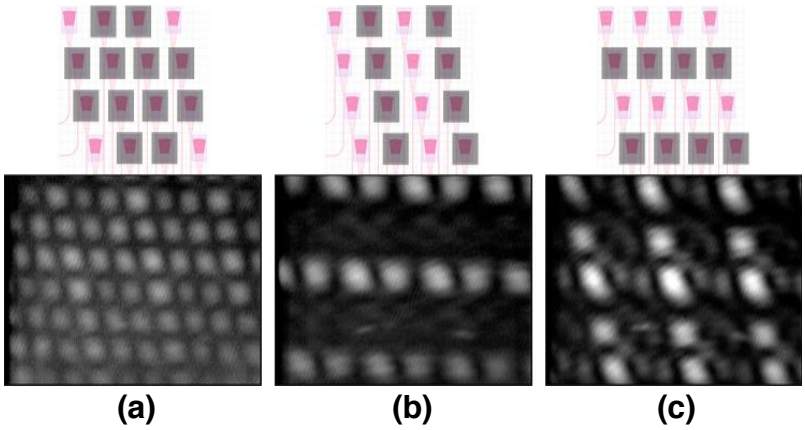

Fig. 7. Top: the OPA element radiation status (only highlighted elements are radiating), bottom: the far-field pattern. (a) The far-field pattern of the OPA when all elements except for the ones at the corners of the array are turned off , (b) the far-field pattern of the OPA when elements on every other columns are turned off, and (c) the far-field pattern of the OPA when all elements on every other rows are turned off.

image and is used to guide the gradient descent optimizer. In each iteration, the gradient of the error is calculated by perturbing the current of each phase shifter and observing the changes in the captured pattern as well as the error. At the end of each iteration, the currents of the phase shifters are modified by a small amount in the opposite direction of the gradient. In practice, it was observed that if only a single lobe of the OPA pattern is used for error calculations, the gradient descent leads to reasonably accurate results. Once the error between the actual image and the desired simulated image becomes smaller than a pre-programmed threshold, the current settings for all modulators are saved for the target steering angle and the system start optimization for another target angle. The process continues until the optimized current settings for all desired steering angles are saved in a look-up table. To enable the fastest possible operation speed, for any steering angle input to the OPA, the current settings are instantly loaded from the look-up table to all modulators. The flowchart of the optimization process is depicted

#234944 Received 13 Apr 2015; revised 23 Jun 2015; accepted 10 Jul 2015; published 4 Aug 2015
© 2015 OSA

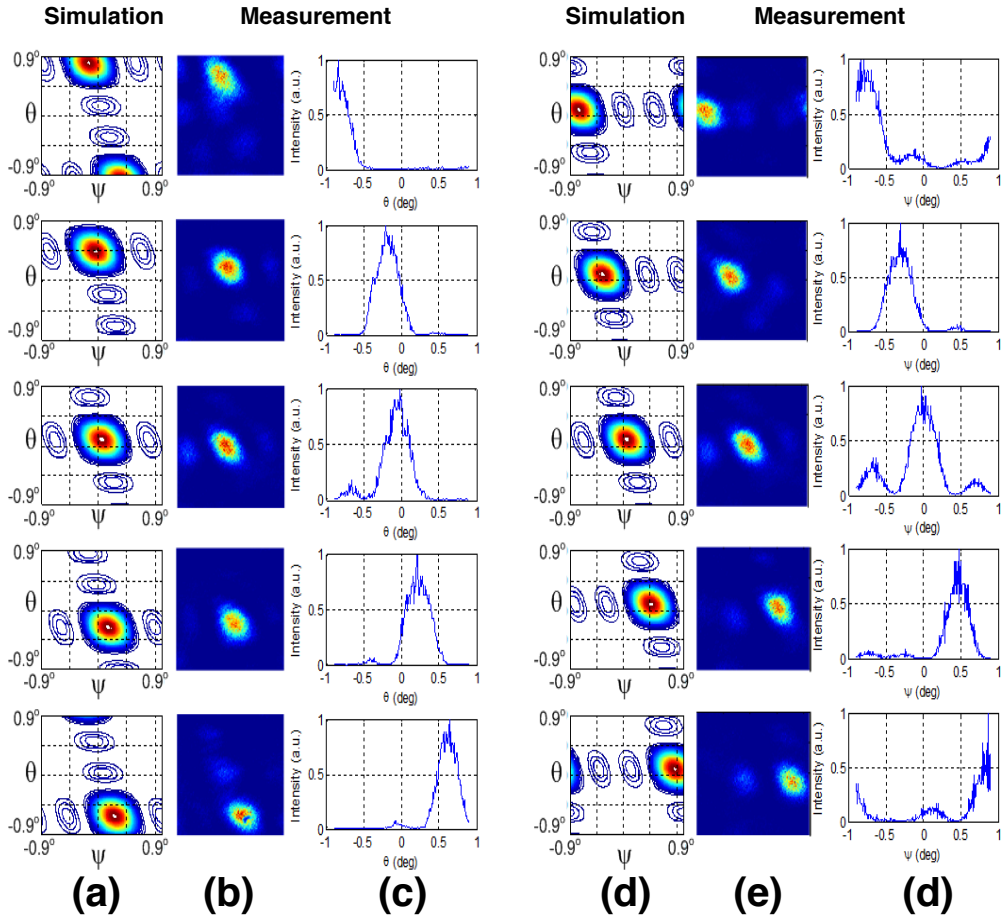

Fig. 8. The vertical beam steering; (a) simulation, (b) measurement, and (c) far-filed pattern cross section. The horizontal beam steering;(d) simulation, (e) measurement, and (f) far-filed pattern cross section.

in Fig. 5.

One important undesired effect in the optimization process is the noise of the IR camera. In order to overcome this effect, in the calibration phase, multiple images were captured and the final image was formed by averaging these images.

5. Measurement results and image and video projection

The nanophotonic projector chips were fabricated in IME silicon-on-insulator technology node [16] where silicon-on-insulator wafers with a $0.22\mu m$ top silicon layer and $2\mu m$ buried oxide are used. Three levels of silicon etching were available. The pixels are grating couplers with about 40% coupling efficiency that were designed using two levels of etching. The Average optical loss of 500nm wide and 220nm thick silicon waveguide is about 1.8dB/cm. No post processing was performed on the fabricated chips. The fabricated chips where mounted on a printed circuit board (PCB) and electrically connected to it using bond wires. No temperature control was required. A commerically available DFB laser emitting 3mW at $\lambda_0 = 1550nm$ is used for all measurements. All measurements have been carried out at the room temperature.

#234944 Received 13 Apr 2015; revised 23 Jun 2015; accepted 10 Jul 2015; published 4 Aug 2015
© 2015 OSA

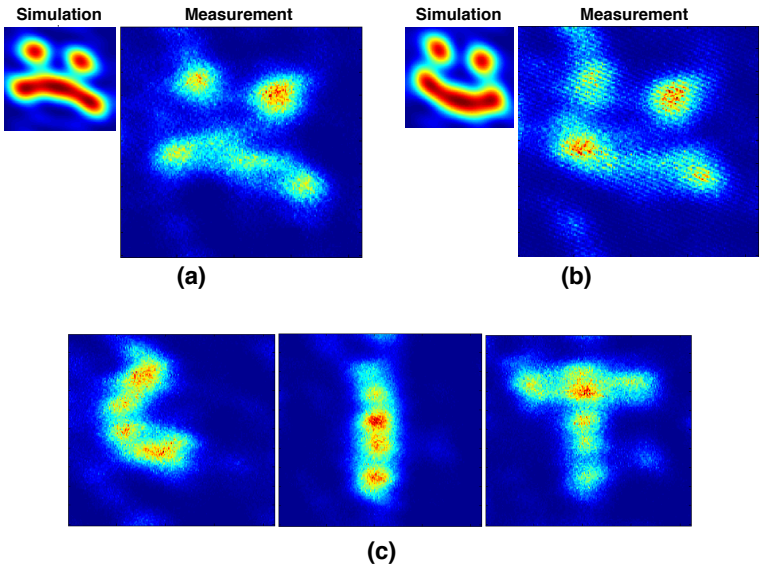

Fig. 9. Projected images by fast vector scan of the beam spot; (a) smiley face (simulation on left), (b)sad face (simulation on left), and (c) individual letters of CIT (California Institute of Technology).

As discussed in section 4, due to process variations, it is not possible to accurately predict the amount of the phase shift and insertion loss introduced by the p-i-n modulator for a given current setting. Therefore, the OPA pattern for certain current setting may deviate from the expected pattern. Figure 6(a) shows the pattern of the OPA for zero relative phase setting ($\Delta\phi_m = \Delta\phi_n = 0$) captured using FJW View-R-Scope 85400A IR camera placed a few centimeters away from the OPA chip surface. The image distortion introduced by the effect of process variation is significantly reduced after gradient decent optimization is performed (Fig. 6(b)).

Since the insertion loss of p-i-n modulators can be controlled by the amount of the modulator current, it is possible to control the radiating power of individual OPA elements. In the extreme case, an OPA radiating element can be effectively turned off by injecting 20mA of current to the corresponding p-i-n modulator. Figure 7(a) shows the far-field pattern of the OPA when all OPA elements are turned off except for the elements located at the corner of the array. As expected, the beam spacing is reduced. In a different experiment, the elements located on every other column are turned off. In this case, the vertical lobe spacing is increased while the horizontal spacing remains the same. This is depicted in Fig. 7(b). Similarly, as shown in Fig. 7(c), when the elements on every other row are turned off, the horizontal lobe spacing increases.

In order to demonstrate reliable two-dimensional beam steering, after calibration phase, gradual beam steering in both vertical and horizontal directions has been performed which is compared with the simulated pattern in Fig. 8. As shown, the OPA is capable of two-dimensional beam steering over full vertical and horizontal lobe spacing periods. Figures 8(a) and 8(b) show that the measured vertical beam spot movements are in close agreement with the corresponding simulations. Figure 8(c) shows the cross-section of the measured far-field pattern of the OPA. Similarly, Figs. 8(d), 8(e), and 8(f) show the horizontal beam spot movements. Note that the vertical beam steering has some small horizontal shift due the parallelogram lattice structure of the array.

After the calibration is performed, the OPA can be used as a projector by quick vector or

#234944 Received 13 Apr 2015; revised 23 Jun 2015; accepted 10 Jul 2015; published 4 Aug 2015
© 2015 OSA

raster scan of the beam spot on the screen. Figures 9(a) and (b) show the simulated and projected smiley and sad faces that are formed by fast vector scan of the beam spot, respectively. The entire image was captured in real time with a single snapshot of the IR camera. Figure 9(c) shows the projected images of letters 'C', 'I', and 'T' for California Institute of Technology.

6. Conclusion

We have reported an integrated projection system based on a two-dimensional optical phased array where p-i-n phase shifters with 200MHz bandwidth are used for rapid beam steering which enables real time projection of an image by fast vector scanning. We have implemented an optimization algorithm to compensate for the phase dependent attenuation of the p-i-n modulators. Using fast vector scan of the beam spot, images were formed and recorded within a single snapshot of the IR camera. This work is a step towards utilizing integrated photonics platforms in realization of integrated projection systems with large number of emitters making low-cost high performance integrated projectors available for varieties of applications in near future.

Acknowledgments

We thank OpSIS foundry for the fabrication of the chips and Profs. Micheal Hochberg and Tom Baehr-Jones from University of Delaware for valuable discussions on fabrication process.

#234944 Received 13 Apr 2015; revised 23 Jun 2015; accepted 10 Jul 2015; published 4 Aug 2015
© 2015 OSA